Chemical Engineering Journal 461 (2023) 141951

Contents lists available at ScienceDirect

Chemical Engineering Journal

journal homepage: www.elsevier.com/locate/cej

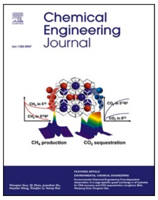

Formation of Fe(IV) over a wide pH range via iron-carbon composite-catalyzed persulfate activation

Hong Li [a], Rongliang Qiu [b,c], Yetao Tang [b,d], Xiaoguang Duan [e], Yanling Gu [f], Hailan Yang [a], Qiang Chen [a], Zihan Shu [a], Ling Xiang [a], Shaobo Liu [g,h], Xiaofei Tan [a,*]

[a] College of Environmental Science and Engineering, Hunan University and Key Laboratory of Environmental Biology and Pollution Control (Hunan University), Ministry of Education, Changsha 410082, PR China
[b] School of Environmental Science and Engineering, Sun Yat-sen University, Guangzhou 510275, PR China
[c] Guangdong Provincial Key Laboratory of Agricultural & Rural Pollution Abatement and Environmental Safety, College of Natural Resources and Environment, South China Agricultural University, Guangzhou 510642, PR China
[d] Guangdong Provincial Key Lab of Environmental Pollution Control and Remediation Technology, Sun Yat-sen University, Guangzhou 510275, PR China
[e] School of Chemical Engineering and Advanced Materials, The University of Adelaide, Adelaide, SA 5005, Australia
[f] College of Materials Science and Engineering, Changsha University of Science and Technology, Changsha 410114, PR China
[g] School of Architecture and Art, Central South University, Changsha 410083, PR China
[h] School of Metallurgy and Environment, Central South University, Changsha 410083, PR China

ARTICLE INFO

Keywords:
Low-temperature pyrolysis
Iron-carbon composites
Persulfate
High-valent iron
Potassium butyl xanthate

ABSTRACT

Fe(IV) is typically formed under acidic or neutral conditions while its formation mechanism and impacts on pollutant decomposition have been overlooked, particularly in persulfate (PS) systems. In this study, an iron-carbon composite (Fe-BC250) was prepared at a low-temperature (250 °C) to explore the PS activation and Fe (IV) formation processes under a wide range of pH conditions. Fe(IV) was the main reactive species in the iron-carbon composite/PS system, and Fe species promoted the graphitization of biochars. The existence of Fe(IV) in the Fe-BC250/PS system was identified by *in situ* Raman, Mössbauer spectrum, and methyl phenyl sulfoxide probe (PMSO) experiments. Under alkaline conditions, the solution pH decreased because hydrolyzed Fe^{2+} generated H^+, and surface Fe(II) reacted with PS to form Fe(IV). The Fe-BC250/PS system was superior in removing contaminants under alkaline conditions compared to the Fe^{2+}/PS system, due to the slow release of Fe^{2+} from Fe-BC250. This study offers new insights into the Fe(IV) formation mechanism in biochar/PS systems under a wide range of pH conditions and provides a theoretical basis for applying low-cost iron-carbon composites in water treatment.

1. Introduction

Highly efficient and low-cost iron-carbon composites are widely regarded as satisfactory persulfate (PS) activators [1]. The valence state of iron can also be well manipulated during thermal treatment [2]. For instance, zero-valent iron (Fe^0) or iron oxides are obtained under high-temperature pyrolysis (>400 °C) and reduction [3,4], resulting in iron-carbon composites with high catalytic performance (see related research papers listed in Table S1). However, iron-carbon composites pyrolyzed at low temperatures (<300 °C) are less explored. Given the low energy consumption and high yields of products from low-temperature pyrolysis, iron-carbon composites pyrolyzed at low temperatures have the advantages of environmental friendliness compared with conventional iron-based biochar.

Sulfate radicals ($SO_4^{\bullet -}$), hydroxyl radicals ($HO^{\bullet}$), and singlet oxygen ($^1O_2$) are the commonly detected reactive oxygen species (ROS) in iron-based catalysts/PS systems [5]. High-valent iron species (especially Fe (IV)) have recently been detected as contributors to advanced oxidation processes (AOPs) [6–8]. Although the redox potential of Fe(IV)(E_0(Fe (IV)/Fe(III)) = 2.0 V) is lower than that of $HO^{\bullet}$($E_0(HO^{\bullet}/H_2O) = 2.72$ V) and $SO_4^{\bullet -}$($E_0(SO_4^{\bullet -}/SO_4^{2-} = 2.52–3.08$ V), the Fe(IV) pathway has an anti-interference capacity to the background factors (inorganic anions and natural organics) and can selectively degrade pollutants in actual wastewater [9,10]. To the best of our knowledge, Fe(IV) is mainly produced from Fe^{2+} or some solid iron-based catalysts oxidized by peroxides (Table S2). The presence of Fe(IV) can be evidenced by

---

[*] Corresponding author.
E-mail address: tanxf@hnu.edu.cn (X. Tan).

https://doi.org/10.1016/j.cej.2023.141951
Received 28 November 2022; Received in revised form 17 January 2023; Accepted 14 February 2023
Available online 19 February 2023

various characterizations, including Mössbauer spectroscopy and *in situ* Raman spectroscopy [11–13]. Furthermore, several studies show that Fe(IV) is only formed in acidic or neutral solutions [14,15], whereas few studies have explored the formation of Fe(IV) over a wide pH range, particularly in alkaline environments.

As a widely used collector in flotation, potassium butyl xanthate (BX) has become a major organic pollutant in mineral processing wastewater [16]. Some studies report that Fe(IV) can couple with and degrade the S atoms in pollutants [10,13]. Based on its sulfur-containing groups, BX was selected as the target contaminant in this study to explore novel pathways for removing sulfur-containing pollutants in the Fe-BC250/PS system.

In this study, we prepared an iron-carbon composite at a low temperature (250 °C). The physical and chemical properties of the composites were investigated, and their catalytic performances were evaluated. Active species were identified using various methods, including quenching experiments, methyl phenyl sulfoxide probe (PMSO) probe experiments, electron paramagnetic resonance (EPR), electrochemical analysis, *in situ* Raman spectroscopy, and Mössbauer spectroscopy. Fe(IV) formation was further studied over a wide pH range, and the mechanism of the initial fast oxidation stage during BX degradation was investigated. As such, our work provides novel insights and a theoretical basis for the future application of low-temperature iron-carbon composite materials, and offers new perspectives on the study of Fe(IV) in AOPs.

2. Materials and methods

2.1. Materials and chemicals

Details of materials and chemicals are provided in Text S1.

2.2. Preparation of low-temperature iron-carbon composites

The iron-carbon composite was pyrolyzed at a low temperature using a facile method. Waste wood shavings were selected as biomass feedstocks. The wood shavings were crushed and passed through a 100-mesh sieve. Then, the sieved wood shavings and ferric chloride hexahydrate ($FeCl_3·6H_2O$) were mixed at a mass ratio of 3.6:1 and ball-milled for 40 min at 300 rpm. The low-temperature iron-carbon composite was obtained from the pyrolyzed mixture in a tube furnace at 250 °C for 1 h under N_2 flow, named Fe-BC250. The Fe-BC250 was weighed to obtain an 80 % yield. The solid products obtained from the pyrolysis of $FeCl_3·6H_2O$ or ball-milled biomass in a tube furnace at 250 °C were denoted as $FeCl_3·6H_2O$250 and BC250, respectively. Information on the characterization of the materials is provided in Text S2.

2.3. Batch experiment

The catalytic properties of the materials prepared for degradation of BX were implemented in a 250 mL conical flask containing 0.1 g L^{-1} biochar, 0.1 mmol/L PS, and 20 mg L^{-1} BX, and reacted in a shaker (150 rpm/min) at 25 °C. If not otherwise specified, the solution pH was 6.85. A 3 mL sample was taken at set time intervals and quenched with 30 μL of 1 mol/L sodium thiosulfate pentahydrate, and then filtered through a 0.22 μm PTFE filter. The BX concentration was detected and quantified using a high-performance liquid chromatography (HPLC) (Agilent 1100, USA). The influences of environmental factors, including pH, anions, and natural organic matter, were also studied. All experiments were repeated three times. The active substances were identified by quenching experiments. The electron transfer process of the system was demonstrated by electrochemical tests, and the existence and function of Fe(IV) were confirmed by a PMSO probe experiment, *in-situ* Raman spectroscopy test, and Mössbauer test (as detailed in Text S3-S5).

2.4. Analysis methods

The BX, PMSO, and $PMSO_2$ concentrations were quantified by HPLC equipped with a UV–vis detector using an Extend-C18 (5 μm, 4.6 × 250 mm) column. The mobile phase employed to assess the concentration of BX was acetonitrile and 0.05 mol/L ammonium acetate solution (adjusted pH to 9.5 with ammonia) at a 25:75 vol ratio. The flow rate of 1 mL min^{-1}. BX was identified using the UV mode at 301 nm. The mobile phase (acetonitrile: $H_2O = 2:8$; flow rate:1 mL min^{-1}) was used to quantify the PMSO and $PMSO_2$ concentrations. PMSO and $PMSO_2$ were tested in UV mode at 215 nm. The Fe^{2+} concentration was measured using the 1,10-phenanthroline method on a UV–vis spectrophotometer at 530 nm (Shimadzu, Japan) [17]. The total Fe content was determined using a flame atomic absorption spectrometer (PinAAcle900F, USA). The concentration of the persulfate anion ($S_2O_8^{2-}$) was investigated by potassium iodide spectrophotometry using a UV–vis spectrophotometer at 400 nm. Free radical species were measured on an EPR instrument (Bruker emxplus-6/1, Germany).

3. Results and discussion

3.1. Characterizations of low-temperature iron-carbon composites

Phase identification of Fe-BC250 was performed by X-ray diffraction (XRD) analysis to obtain material composition information (Figure S1). The BC250 sample exhibited broad diffraction peaks at 15.6° and 22.1° of 2θ values, which could be ascribed to the amorphous carbons in biochar [18]. In comparison, for Fe-BC250, the peak was weaker, manifesting a significant change in its intrinsic carbon characteristics. Six new diffraction peaks were observed, which can be indexed to $FeCl_2·4H_2O$ (JCPDS: No.71-0668) of (1 0 0), (0 0 2), (1 2 0), (1 0 2), (1 2 2), and (0 2 3). Additionally, the $FeCl_2$ signal was observed in the Mössbauer spectra (Fig. 4b-d). The $FeCl_3·6H_2O$250 XRD pattern illustrates the classic FeOCl (JCPDS: No.74-1369) phase. 11.1° is indexed to the (0 1 0) facet, and the diffraction peak at 26.3° arises from the (1 1 0) plane. $FeCl_2$ was only formed when biomass and $FeCl_3·6H_2O$ were co-pyrolyzed, which may be due to the reduction of $FeCl_3·6H_2O$ by the gas generated during biomass pyrolysis, which is also consistent with previous reports [2].

The morphologies and microstructures of the catalysts were explored using a scanning electron microscope (SEM). BC250 exhibited a blocky morphology (Figure S2a-b), and there were nano-sized particles on the surface of Fe-BC250 (Figure S2c-f). The detailed chemical composition of Fe-BC250 was further analyzed using elemental mapping (Figure S3) and EDS images (Figure S4). Figure S3 shows that Fe-BC250 had C, O, Cl, and Fe elements. Additionally, the EDS results (Table S3) show that the Cl and Fe atomic ratio in Fe-BC250 was approximately 2:1, further proving the formation of $FeCl_2$, which coincides with the XRD results. BC250 showed an amorphous morphology (Figure S5a), while Fe-BC250 featured a layered structure (Figure S5b). This may be because the added Fe promoted graphitization generation [19]. Lattice fringes with a spacing of approximately 0.2138 nm can also be seen in Figure S5c, which match well with the (1 2 2) plane of $FeCl_2·4H_2O$.

The surface chemical composition of iron-carbon composites was investigated by X-ray photoelectron spectroscopy (XPS), and the valence state information of the elements was obtained (Figure S6). The full Fe-BC250 spectrum confirmed the existence of C, O, Fe, and Cl (Figure S6h). The Cl 2p spectrum could be deconvoluted into two peaks, 198.6 eV and 200.3 eV, for Fe-Cl (Figure S6g) [20]. The content of Cl^- in the test system was very low and, therefore, had little effect on the catalytic oxidative degradation reaction. The C 1 s spectrum was divided into four types of peaks, corresponding to C—C, C—O, O—C═O, and C (π-π*), respectively (Figure S6a-b). Among them, the C—C proportion was the highest (71.58 %). The relative C—C intensity decreased with increased pyrolysis temperatures, while the C—O content increased due to the progressive aromatic structure condensation at higher temperatures [21]. The 284.8 eV peak corresponding to sp^2 hybridized carbon was observed for Fe-BC250. The 284.8 eV peak corresponding to sp^2 hybrid carbon was also confirmed to be graphitic carbon in Fe-BC250 [22]. After catalytic oxidative degradation, the percentage of sp^2 hybrid carbon decreased from 71.6 % to 67.7 %, suggesting that the graphitic structures in Fe-BC250 might participate in the reaction process. Two peaks were fitted in the O 1 s spectrum, corresponding to C—O and C═O, in which the content of C—O was reduced from 59.1 % to 46.27 %, demonstrating that these functional groups are potential active sites in AOPs (Figure S6c-d). The same conclusion was obtained by monitoring the changes of oxygen-containing functional groups before and after the reaction by Fourier transform infrared (FTIR) spectroscopy (Figure S7a). Two peak types were decomposed in the Fe 2p spectra, and 711 eV and 723.4 eV were assigned to $Fe2p_{3/2}$ ($FeCl_2$) and $Fe2p_{1/2}$ ($FeCl_2$) peaks, which supported the XRD and EDS findings (Figure S6e-f). After the reaction, the Fe(III) proportion increased significantly, while the Fe(II) content decreased, revealing that Fe(II) was involved in the catalytic degradation process.

The surface defect of the prepared material was probed by Raman spectroscopy. The appearance of the G-band was related to the stretching vibration of sp^2 carbon [19]. Figure S7b showed that the G-band appeared in Fe-BC250, indicating the presence of graphitic carbon, while no G-band occurred in BC250. Thus, adding Fe promoted the formation of graphitized structures. After the catalytic oxidative degradation reaction, the G-band disappeared. In contrast, the G-band did not disappear for Fe-BC250 in pure water without persulfate. Therefore, graphitic carbon played an essential role in persulfate activation. The process of pollutant degradation loses electrons while the active species gains them, and the graphitized carbon may be able to accelerate the shuttling of electrons during this process of electron exchange.

3.2. Catalytic removal of BX in different systems

Fe-BC250 exhibited poor adsorption toward BX (Fig. 1a) due to its small specific surface area (SSA) of 3.78 m^2/g. The BX removal rate in the PS-alone system was 2.8 %, indicating that PS had a poor oxidation effect on BX. The adsorption capacity of Fe-BC250 at different pH values was also investigated, and Fe-BC250 adsorbed poorly on BX at pH 6–10 (Figure S18). Compared to BC250, Fe-BC250 exhibited enhanced BX removal rates in the PS system, reaching 94.6 % in 30 min. Although the $FeCl_3{\cdot}6H_2O250$/PS system reached a similar BX-removal efficiency in 30 min compared to the Fe-BC250/PS system, the $k_{obs,BX}$ in the $FeCl_3{\cdot}6H_2O250$ /PS system was only 0.09 min^{-1}, which was much lower than that of the Fe-BC250/PS system (0.27 min^{-1}) (Figure S8). These results show that the Fe-BC250/PS system exhibited good performance with respect to PS activation and BX degradation. The Fe-BC250/PS system exhibited better catalytic degradation performance for BX for the following reasons: first, $FeCl_3{\cdot}6H_2O250$(FeOCl) activates oxidants through the free radical pathway to degrade organic matter [23–25], and Fe(IV) is the dominant pathway of the degradation of pollutants containing sulfur functional groups [10,13]; second, the release of Fe^{2+}

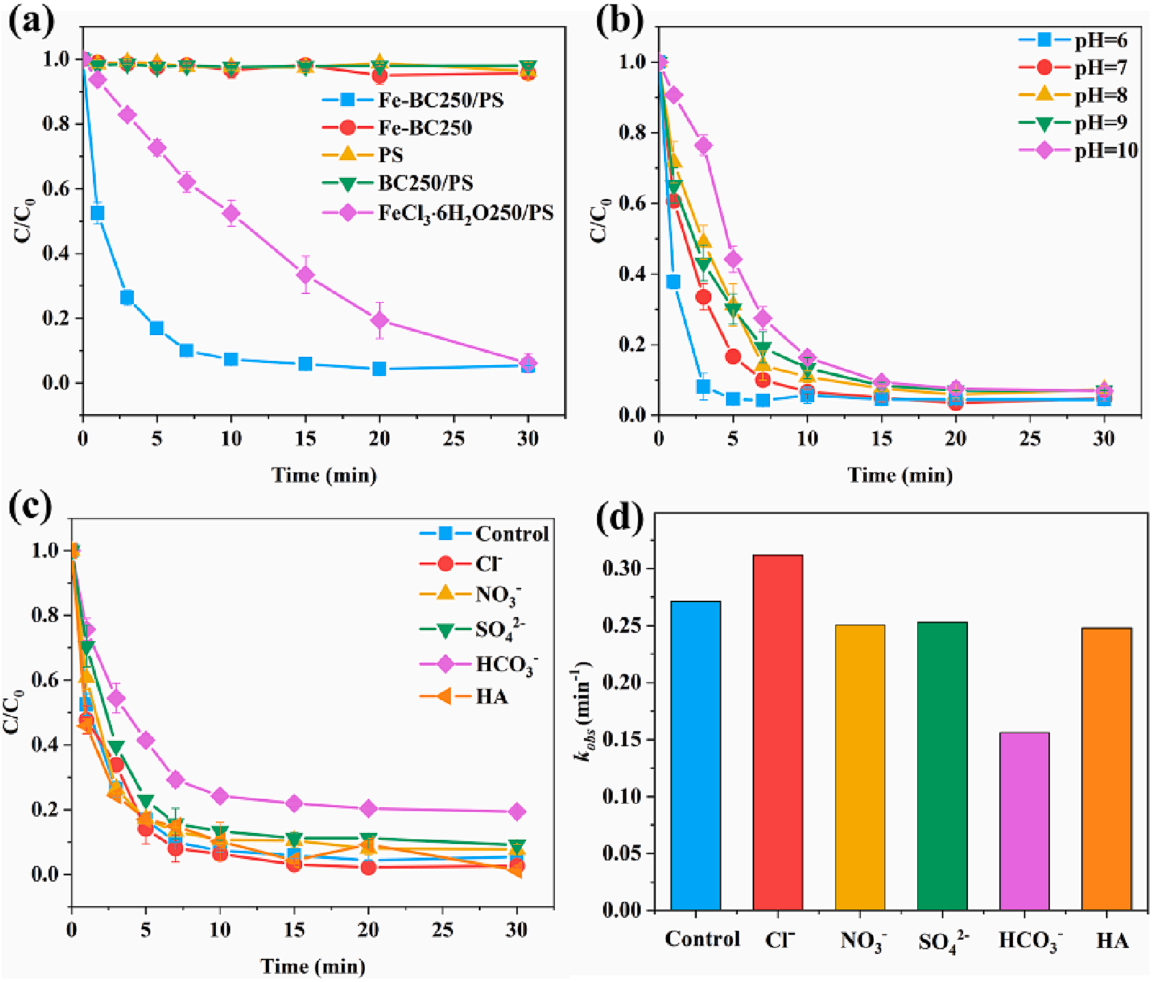

Fig. 1. BX removal efficiency in the different systems (a); BX degradation under different initial pH conditions (b); Influences of coexisting anions and humic acids on BX removal in the Fe-BC250/PS system (c). The apparent rate constant (k_{obs}) of BX removal of c (d). ([BX] = 20 mg/L, [Fe-BC250/BC250/ $FeCl_3{\cdot}6H_2O250$] = 0.1 g/L, [PS] = 0.1 mmol/L, [Cl^-] = 4 mmol/L, [NO_3^-] = 2 mmol/L, [SO_4^{2-}] = 2 mmol/L, [HCO_3^-] = 0.1 mmol/L, [HA] = 10 mg/L, T = 25 °C).

in Fe-BC250 is a homogeneous reaction, and the rate of degradation is faster than that of non-homogeneous reactions.

3.3. *Effect of water matrix*

The performance of advanced oxidation systems can be affected by solution pH [26,27]. Thus, the pH-dependent behavior of the Fe-BC250/PS system was surveyed. Fig. 1b illustrates that the BX degradation efficiency decreased slightly when the initial solution pH was increased from 6 to 10. Via calculating the apparent rate constants of BX removal under different pH conditions. As the initial solution pH increased from 7 to 10, $k_{obs,\ BX,}$ decreased from 0.30 min^{-1} to 0.17 min^{-1}. As the reaction rate greatly accelerates at pH 6, most studies have been conducted under acidic conditions. Thus, we did not perform further experiments below pH 6. Furthermore, as the solution pH increases, the catalytic oxidative degradation reaction is inhibited, and, therefore, we do not discuss strongly alkaline environments (pH $>$ 10). BX degradation was favorable under acidic conditions, whereas the BX removal rate was inhibited under alkaline conditions. This may be related to the poorer catalytic performance of Fe(II) under alkaline conditions than under acidic condition.

Considering the ubiquitous distribution of inorganic anions and natural organic matter in mine wastewater, the effects of these background species on BX degradation were investigated (Fig. 1c). The coexistence of Cl$^-$ promoted BX degradation, and $k_{obs,\ BX,}$ of BX increased to 0.31 min^{-1} in 30 min, which may be attributed to the fast reaction between Cl$^-$ and Fe(IV), which further forms chlorine-containing active substances. The redox potentials of chlorine radicals such as Cl$^{\bullet}$ and Cl$_2^{\bullet-}$ are 2.4 V and 2.0 V, respectively (Eqs. (1)) [28], which increased the BX removal efficiency. In contrast, the existence of HCO$_3^-$ inhibited BX degradation for the following reasons: (i) HCO$_3^-$ and SO$_4^{\bullet-}$ react to generate HCO$_3^{\bullet-}$, but the redox potential of SO$_4^{\bullet-}$ is much higher than that of HCO$_3^{\bullet-}$ [29]; (ii) HCO$_3^-$ provides an alkaline environment that inhibits pollutant degradation; (iii) HCO$_3^-$ undergoes a double hydrolysis reaction with Fe^{2+} to generate Fe(OH)$_2$, which is oxidized to form Fe(OH)$_3$, and Fe^{2+} is precipitated, which reduces the degradation rate of pollutants. By calculating the apparent rate constants of BX removal under different conditions, NO$_3^-$, SO$_4^{2-}$, and humic acid (HA) had little impact on the apparent rate constant of BX.

$$Cl^{\cdot}+Cl^{-}\rightarrow Cl_2^{-} \tag{1}$$

The operational stability of Fe-BC250 was also evaluated (Figure S9a). After each operation, only 0.1 mmol/L PS and 20 mg/L BX were added to the system. After three cycles, the Fe-BC250/PS system still had a good removal effect on BX. These results show that the stability of Fe-BC250 was satisfactory. The slower reaction rate in the subsequent cycles may be related to the disappearance of the G band in the first experimental cycle. Additionally, the application effect of the Fe-BC250/PS system in real water was evaluated using water from the mining area in Guangxi, China (Table S4), to which 20 mg/L BX was added (Figure S9b). Compared with the removal rate of BX in ultrapure water (94.6 %), the degradation rate of BX in the mining area wastewater after 30 min was 92.3 %, which was only slightly inhibited, indicating that Fe-BC250/PS has the potential for practical application.

3.4. *Active species identification*

To corroborate the reactive species in the catalytic oxidation degradation, quenching and EPR experiments were performed. In the Fe-BC250/PS/DMPO and Fe-BC250/PS/TEMP systems, the signals of

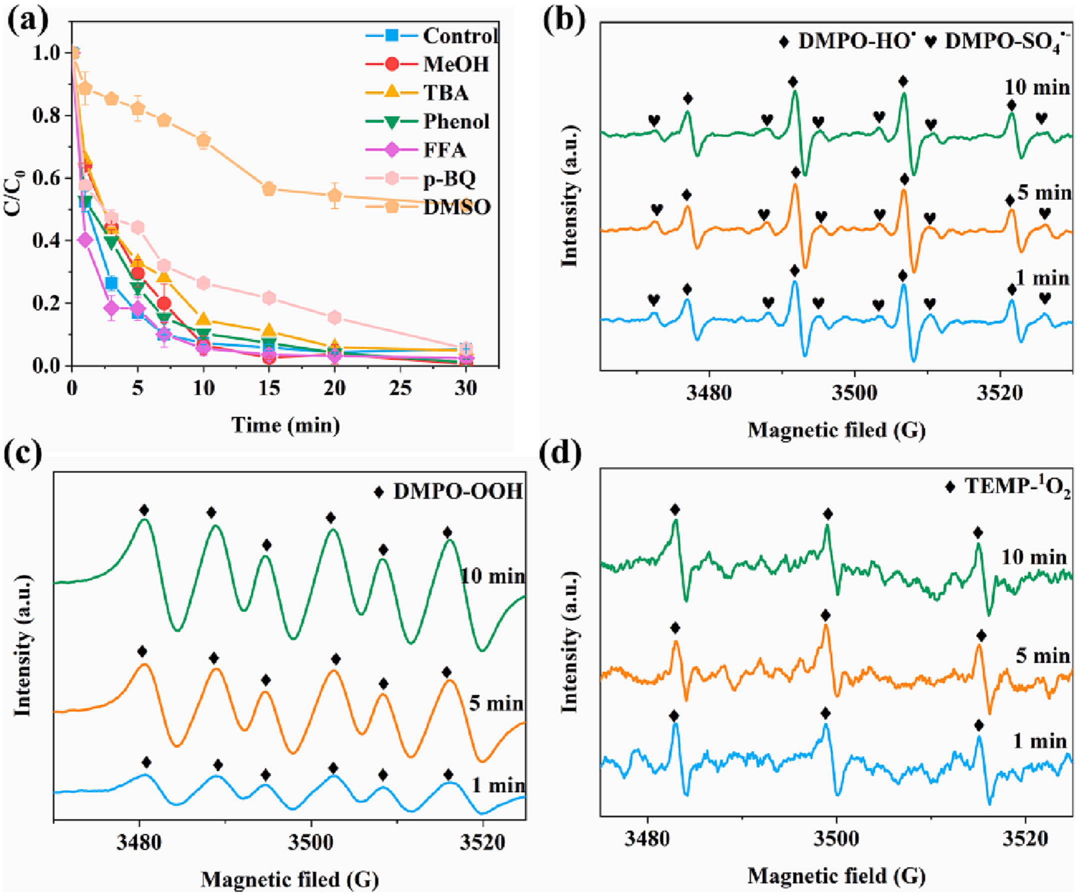

Fig. 2. Quenching experiments of the Fe-BC250/PS system with different scavengers (a), and EPR spectra in the Fe-BC250/PS system (b-d). ([BX] = 20 mg/L, [Fe-BC250] = 0.1 g/L, [PS] = 0.1 mmol/L, T = 25 °C, [MeOH, TBA, Phenol, FFA] = 100 mmol/L, p-BQ = 0.2 mmol/L, DMSO = 10 mmol/L).

DMPO-HO$^{\bullet}$, DMPO-SO$_4^{\bullet-}$, and TEMP-^{1}O$_2$ were detected, but the intensity of the signals remained unchanged at 1, 5, and 10 min (Fig. 2b and 2d). This result is contrary to many previous reports [18,30]. This illustrates that the generation of HO$^{\bullet}$, SO$_4^{\bullet-}$, and ^{1}O$_2$ in the Fe-BC250/PS system was not sufficient. Thus, the system cannot provide enough ROS for subsequent oxidation reactions, which verifies that HO$^{\bullet}$, SO$_4^{\bullet-}$, and ^{1}O$_2$ are not the primary ROS in the Fe-BC250/PS system. Adding a higher concentration of the quencher than the oxidizer can provide the effect of quenching. Methanol (MeOH) is used as a scavenger for HO$^{\bullet}$ and SO$_4^{\bullet-}$ ($k_{HO\bullet\ +\ MeOH} = 3.2 \times 10^6$ M^{-1}s^{-1}, $k_{SO4\bullet\text{-}\ +\ MeOH} = 9.7 \times 10^8$ M^{-1} s^{-1}) [31], and *tert*-butanol (TBA) is an effective HO$^{\bullet}$ scavenger ($k_{HO\bullet\ +\ TBA} = (3.8\text{–}7.6) \times 10^8$ M^{-1}s^{-1}, $k_{SO4\bullet\text{-}\ +\ TBA} = (4\text{–}9.1) \times 10^5$ M^{-1}s^{-1}). Furfuryl alcohol (FFA) was added as a scavenger for ^{1}O$_2$ ($k_1O_2 + FFA = 1.2 \times 10^8\ M^{-1}s^{-1}$) [32]. When MeOH, TBA, or FFA were added at a molar concentration 1000 times that of PS, there was no inhibitory effect on the BX removal efficiency, indicating that HO$^{\bullet}$, SO$_4^{\bullet-}$, and ^{1}O$_2$ were not the main ROS for BX degradation (Fig. 2a). Superoxide radicals (O$_2^{\bullet-}$) are also detected. Under acidic conditions, O$_2^{\bullet-}$ reacts with hydrogen ions to form peroxy-hydroxyl radicals (HO$_2^{\bullet}$) [29]. Because of its weak oxidizing ability [33], HO$_2^{\bullet}$ was not the main active species in the reaction process. To discern the role of O$_2^{\bullet-}$ in the degradation of BX, P-benzoquinone (p-BQ) was added as a scavenger for O$_2^{\bullet-}$($k_{O2\bullet-\ +\ p\text{-}BQ} = (0.9\text{–}1.0 \times 10^9$ M^{-1}s^{-1}) [34]. When p-BQ at a molar concentration two times that of PS were added, the BX degradation rate was not affected (Fig. 2a). Although the intensity of HO$_2^{\bullet}$ in the EPR signal increased with time, the addition of scavenger did not affect the degradation of BX in the quenching experiments. Therefore, HO$_2^{\bullet}$ was not the main ROS for BX degradation.

To further exclude the effect of surface radicals, more hydrophobic phenol ($k_{HO\bullet\ +\ phenol} = 6.6 \times 10^9$ M^{-1}s^{-1}, $k_{SO4\bullet\text{-}\ +\ phenol} = 8.8 \times 10^9$ M^{-1}s^{-1}) was used to scavenge the surface free radical. In the case of phenol at a molar concentration 1000 times that of PS, the BX removal rate was not affected. Thus, surface free radicals did not play a major role in the Fe-BC250/PS system. Dimethyl sulfoxide (DMSO) is used as a scavenger for Fe(IV) [35,36]. In the case of DMSO at a molar concentration 100 times that of PS, the BX removal notably decreased from 94.6 % to 48.7 % in 30 min, indicating that Fe(IV) was the primary ROS for BX degradation.

Experiments verified that none of the radical oxidation or singlet oxygenation were the main Fe-BC250/PS system pathways for BX degradation. Many recent reports indicate that PS can be activated by carbon-based catalysts to generate non-radical complexes that directly oxidize organic pollutants through electron transfer on the carbon surface [35]. To probe the electron transfer pathway, Fe-BC250 and PS were mixed with pollutants added at different time intervals. As shown in Fig. 3a, when the time interval of the delayed addition of pollutants increased, $k_{obs,\ BX}$ decreased to 0.187 min^{-1}. It has been reported that when the electron transfer pathway is used as the main pathway to degrade pollutants, the addition of pollutants at different time intervals has no effect on the degradation rate [37]. This illustrates that direct electron transfer is not the primary oxidation regime in the Fe-BC250/PS system.

The oxidative pathway was further determined by electrochemical experiments, using electrochemical impedance spectroscopy (EIS), linear sweep voltammetry (LSV), and I-t curves. The EIS results showed that Fe-BC250 had a smaller semicircular diameter than BC250, indicating that Fe-BC250 had a lower impedance and better conductivity. Notably, the improved Fe-BC250 conductivity benefited from the graphitized structure (Fig. 3b). Fig. 3c shows no clear change in current after adding PS and BX. The same result was obtained for the I-t curve

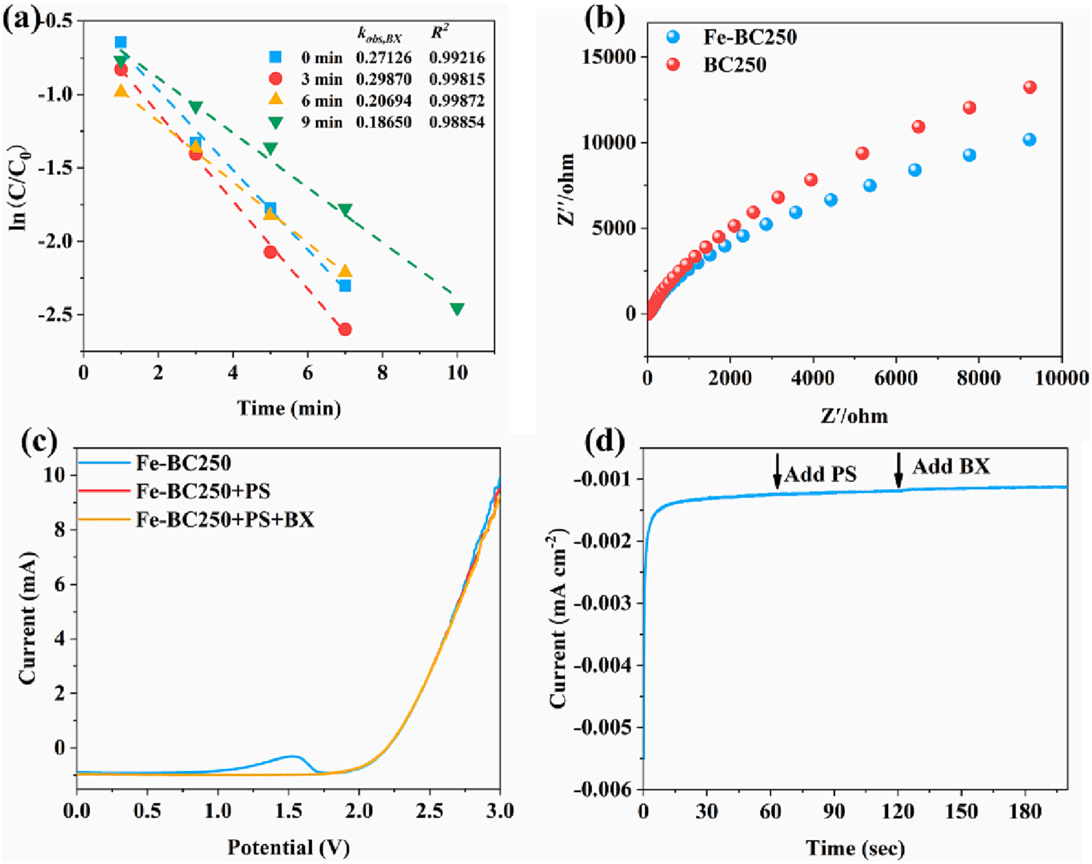

Fig. 3. Removal efficiency of BX based on adding BX at different periods after Fe-BC250 was mixed with PS (a); EIS measurement of catalysts with frequency ranges from 10^{-1} to 10^5 Hz ([Na$_2$SO$_4$] = 0.2 mol/L) (b); LSV under different conditions (0.1 mmol/L PS or both 0.1 mmol/L PS and 20 mg/L BX) (c); I-t curves of Fe-BC250 loaded electrode (d).

(Fig. 3d). These results suggest that electron transfer did not primarily contribute to BX degradation in the Fe-BC250/PS system.

3.5. *Fe(IV) identification*

Recent studies have shown that iron-carbon composites can form Fe(IV) in AOPs [36,38–40]. The Fe(IV) formation was corroborated by *in situ* Raman spectroscopy, and the peaks at 835 cm^{-1} and 1076 cm^{-1} were attributed to the O—O bond of $S_2O_8^{2-}$ in PS. A new peak emerged around 695 cm^{-1} during the reaction, which can be explained by the local oxygen vibrations around Fe^{4+} ions [41]. Fig. 4a reveals that with the increase in PS concentration, the Fe(IV) intensity increased, implying that the Fe(IV) content increased, which further proved the presence of Fe(IV). Additionally, the presence of Fe(IV) was demonstrated by the Mössbauer spectroscopy (Fig. 4b-d). The isomer shifts equal to $-$ 0.17 mm s^{-1} was considered to be the Fe(IV) signal, similar to the Fe(IV) parameter under the spin quantum number $S = 2$ [11,13,42]. The Fe(IV) content showed an upward trend within 2 h, and remained stable from 3 to 24 h (Figure S10).The changes in the iron content of the Mössbauer spectra also indicate the occurrence of the production and consumption of Fe(IV) in the Fe-BC250/PS system.

To verify the presence of Fe(IV), PMSO was selected as the probe because it can only be selectively oxidized to $PMSO_2$ by Fe(IV), while $SO_4^{\bullet-}$ and $HO^{\bullet}$ transform PMSO to biphenyl compounds [14]. PMSO consumption and $PMSO_2$ generation illustrated the existence of Fe(IV) in the Fe-BC250/PS system (Fig. 5a). The $\eta(PMSO_2)$ value (molar ratio of $PMSO_2$ production to PMSO consumption) in the Fe-BC250/PS system was 61.6 %. These results further demonstrate that Fe(IV) played a significant role in BX oxidation in the Fe-BC250/PS system. $PMSO_2$ was still detected in the alkaline solution, suggesting that Fe(IV) still existed under alkaline conditions (Fig. 5b). Some studies have pointed out that $\eta(PMSO_2)$ also decreases with increasing in the solution pH from 3 to 7 [14,43]. There is a high correlation between the amount of $PMSO_2$ generated in the reaction kinetics diagram (Fig. 5c). Therefore, the amount of $PMSO_2$ generated was linearly fitted with $k_{obs,\ BX}$ when the solution was alkaline, and a correlation coefficient of $R^2 = 0.99576$ was obtained (Figure S11). This further proves that Fe(IV) was continuously generated under alkaline conditions.

Moreover, a rapid oxidation stage was observed during the reaction, which is consistent with previous reports [44]. By monitoring the PS concentration, we found that PS was almost completely consumed within 1 min (Figure S12). The subsequent PS concentration fluctuated within a small range. According to the results of the degradation experiments, the BX degradation rate in the Fe-BC250/PS system reached 47.5 % within 1 min. The value of $\eta(PMSO_2)$ within 1 min was 53.1 %, revealing that Fe(IV) primarily contributed to the rapid oxidation during the initial stage.

3.6. *Formation mechanism of Fe(IV) and formation process under alkaline conditions*

To further explore the Fe(IV) formation pathway in the Fe-BC250/PS system, 2,2́-bipyridyl (BPY) was used as a probe compound because of the strong interaction between BPY and Fe(II). Thus, BPY can rapidly form chelate complexes with Fe(II) to prevent the further reaction with PS [45]. When 0.5 mmol/L BPY was added, BX removal in the Fe-BC250/PS system was almost completely inhibited (Fig. 5d) and the BX removal efficiency decreased from 94.7 % to 12.7 %. This verifies the critical role of Fe(II) in PS activation to generate Fe(IV), which subsequently participates in the catalytic degradation of BX (Eqs. (2) and (3)).

$$Fe(II) + S_2O_8^{2-} \rightarrow Fe(IV) + SO_4^{2-} \quad (2)$$

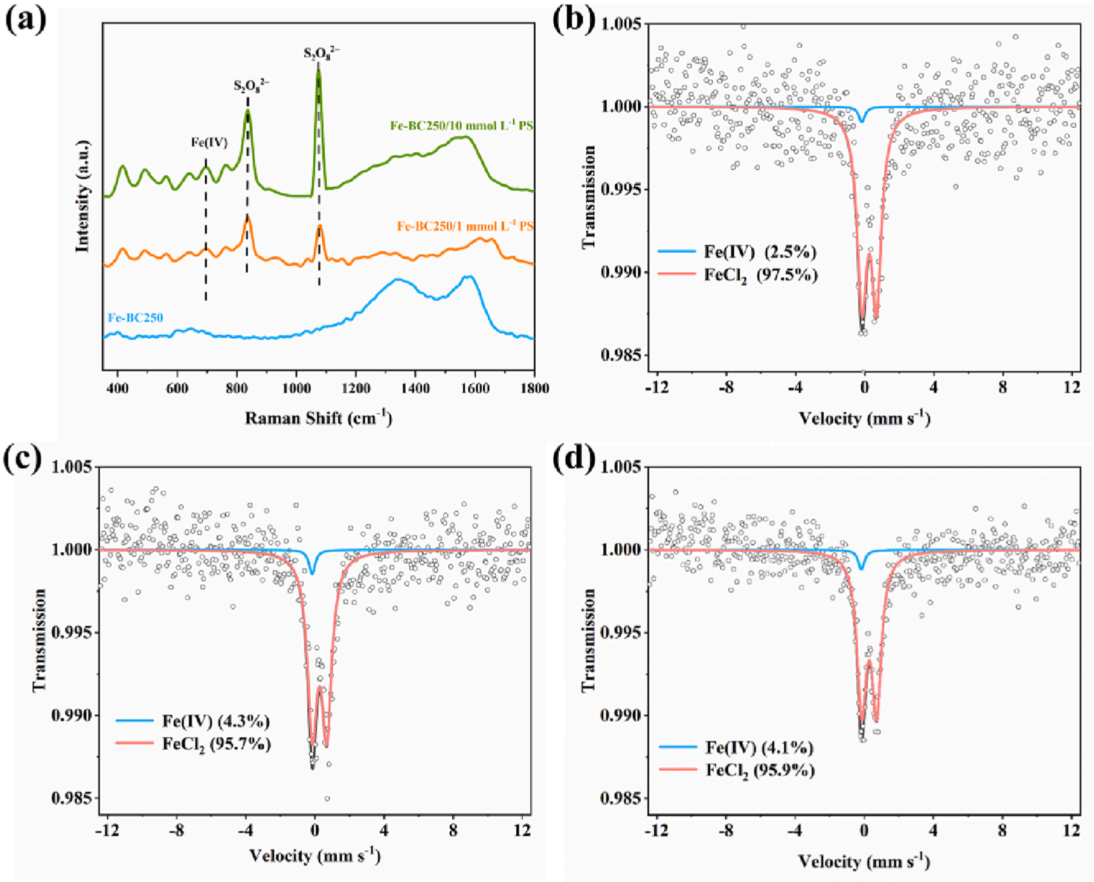

Fig. 4. *In situ* Raman spectroscopy of the Fe-BC250 and Fe-BC250/PS systems (a); Mössbauer spectra of the Fe-BC250/PS system at 1 h (b), 2 h (c), and 3 h (d).

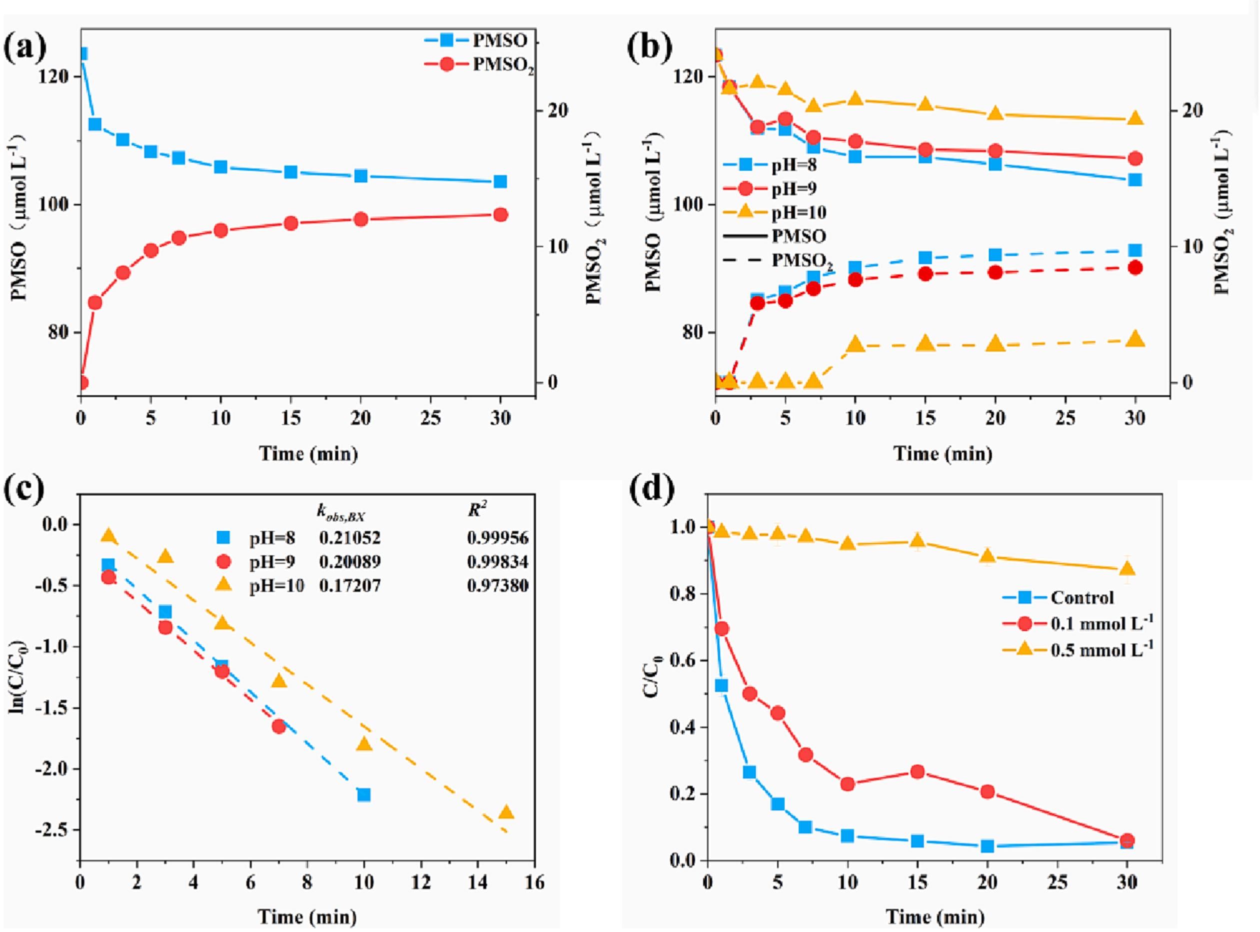

Fig. 5. PMSO consumption and $PMSO_2$ generation in the Fe-BC250/PS system (a); PMSO consumption and $PMSO_2$ generation in the Fe-BC250/PS system under different initial pH of the solution (b); The apparent rate constant for the degradation of BX under the initial solution pH (c); BX degradation with different concentrations of 2,2́-Bipyridyl (BPY) in the Fe-BC250/PS system (d). ([Fe-BC250] = 0.1 g/L, [PS] = 0.1 mmol/L, T = 25 °C, (a, b) [PMSO] = 125 μmol/L, (d) [BX] = 20 mg/L [BPY] = 0.1 or 0.5 mmol/L).

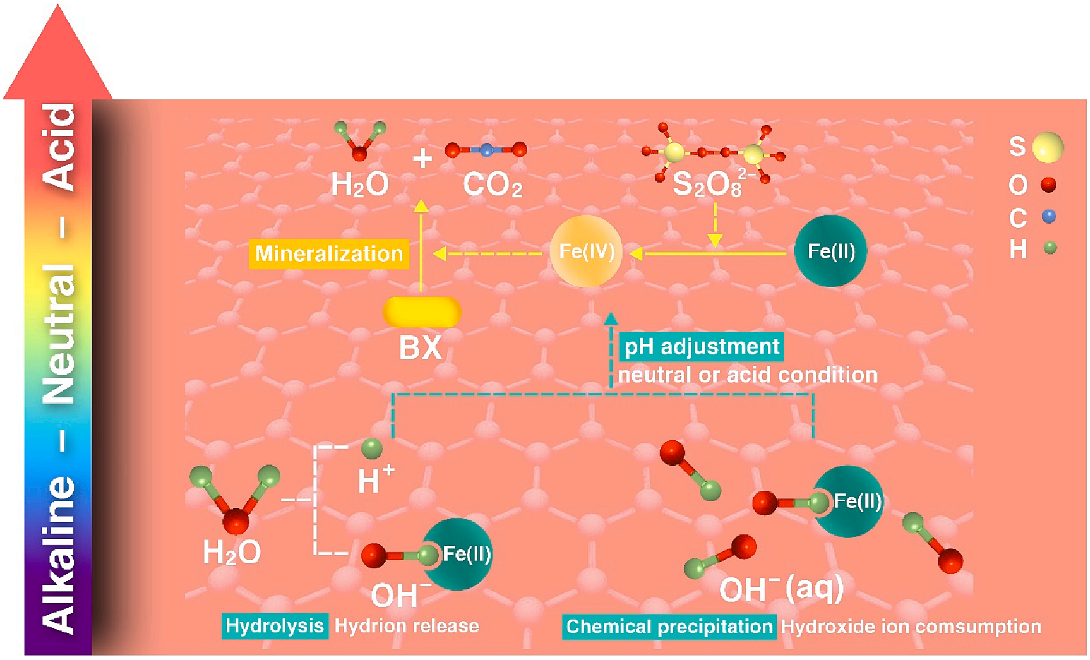

Fig. 6. Mechanism of BX degradation in the Fe-BC250/PS system.

$$\mathrm{Fe(IV)} + \mathrm{BX} \rightarrow \mathrm{Intermediates} + \mathrm{CO_2} + \mathrm{H_2O} + \mathrm{Fe^{3+}} \quad (3)$$

Fe(IV) is typically produced under acidic or neutral conditions [46]. In our experiments, Fe(IV) was still produced in the alkaline solution. We found that the addition of Fe-BC250 changed the solution pH from alkaline to acidic conditions. When the initial solution pH was 8 or 9, the final solution pH decreased to 6.15 after adding Fe-BC250 (Figure S13). These results may also explain why the removal efficiency was similar for the two conditions. In contrast, the addition of BC250 did not significantly alter the solution pH. This suggests that the change in solution pH was caused by Fe^{2+} leached from Fe-BC250, and the solution pH change was attributed to Fe^{2+} hydrolysis and Fe^{2+} combined with OH^- (Fig. 6).

To further study the function of free Fe^{2+} in the reaction process, an equivalent Fe^{2+}+BC250/PS system was constructed. The iron salt added to the Fe^{2+}-BC250/PS system was $FeCl_2{\cdot}4H_2O$. Based on a comparison of the two systems (Figure S14), the Fe-BC250/PS system showed a higher BX removal efficiency. This may be related to the formation of graphitized structures that promote electron shuttling in the catalytic oxidative degradation reaction, thus accelerating the reaction rate. Notably, both the Fe^{2+}+BC250/PS and Fe-BC250/PS systems showed a good removal effect on BX, which indicates that Fe^{2+} plays an important role in the catalytic oxidative degradation reaction. Equivalent Fe^{2+}/PS systems at different pH conditions were also constructed. Notably, the degradation efficiency of BX in the Fe-BC250/PS system was higher than that in the Fe^{2+}/PS system (Fig. 7c), possibly due to the graphitized structure of biochar caused by Fe species. Previous experiments showed that Fe-BC250 has better conductivity compared to BC250 (Fig. 3b), which may accelerate electron shuttling during the reaction, thereby intensifying catalytic oxidation.

Another contributing factor of the Fe-BC250/PS system is the slow-released Fe^{2+} from Fe-BC250. Specifically, when Fe-BC250 was added to the alkaline BX solution, part of the Fe^{2+} was released into the solution and combined with OH^- to produce $Fe(OH)_3$, leading to a lower solution pH. The remaining Fe^{2+} ions can react with PS to form Fe(IV) under acidic conditions. With the addition of BX and PS, the Fe^{2+} content increased, which may be related to the formation of acidic substances after BX degradation, resulting in further decline in pH and a larger amount of Fe^{2+} leaching (Fig. 7b).

The change in the total iron content of the Fe-BC250/PS system is shown in Fig. 7d. The total iron content in the solution increased with the reaction, further confirming the slow release of iron from biochar. The highest concentration of total iron during the whole reaction process was 3.78 mg/L. This illustrates that some Fe(II) remained in Fe-BC250 and contributed to BX oxidation. High solution pH inhibited iron leaching from biochar, and PS can be activated by Fe-BC250/PS in a heterogeneous manner, exhibiting a higher removal rate than the Fe^{2+}/PS system under alkaline conditions.

3.7. Proposed degradation pathway of BX

The BX degradation products were detected by LC-MS (Fig. 8, Figure S15). When the free radical pathway is used as the dominant pathway to degrade BX, the C—O bond in BX is easily broken, resulting in the formation of butanol and CS_2 [46,47]. In view of the analysis of the intermediates, we summarized three degradation pathways: hydroxylation, S—H bond cleavage, and S-radical coupling. It has been reported that organic pollutants are degraded by Fe(IV) through

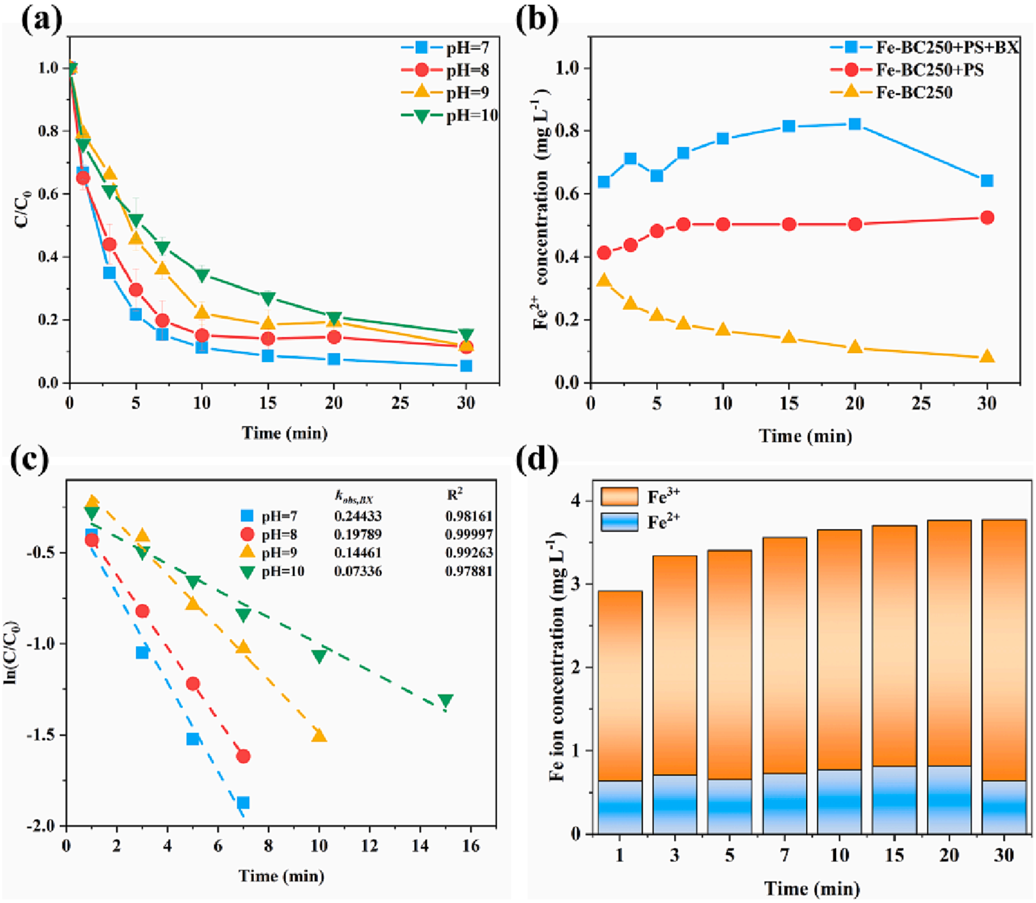

Fig. 7. BX removal in the Fe^{2+}/PS system under different pH conditions (a); Fe^{2+} content in different systems (b); The apparent rate (k_{obs}) of BX removal in the Fe^{2+}/PS system under different initial pH (c) concentration variations of total Fe^{2+} and Fe^{3+} during the reaction in the Fe-BC250/PS system (d).

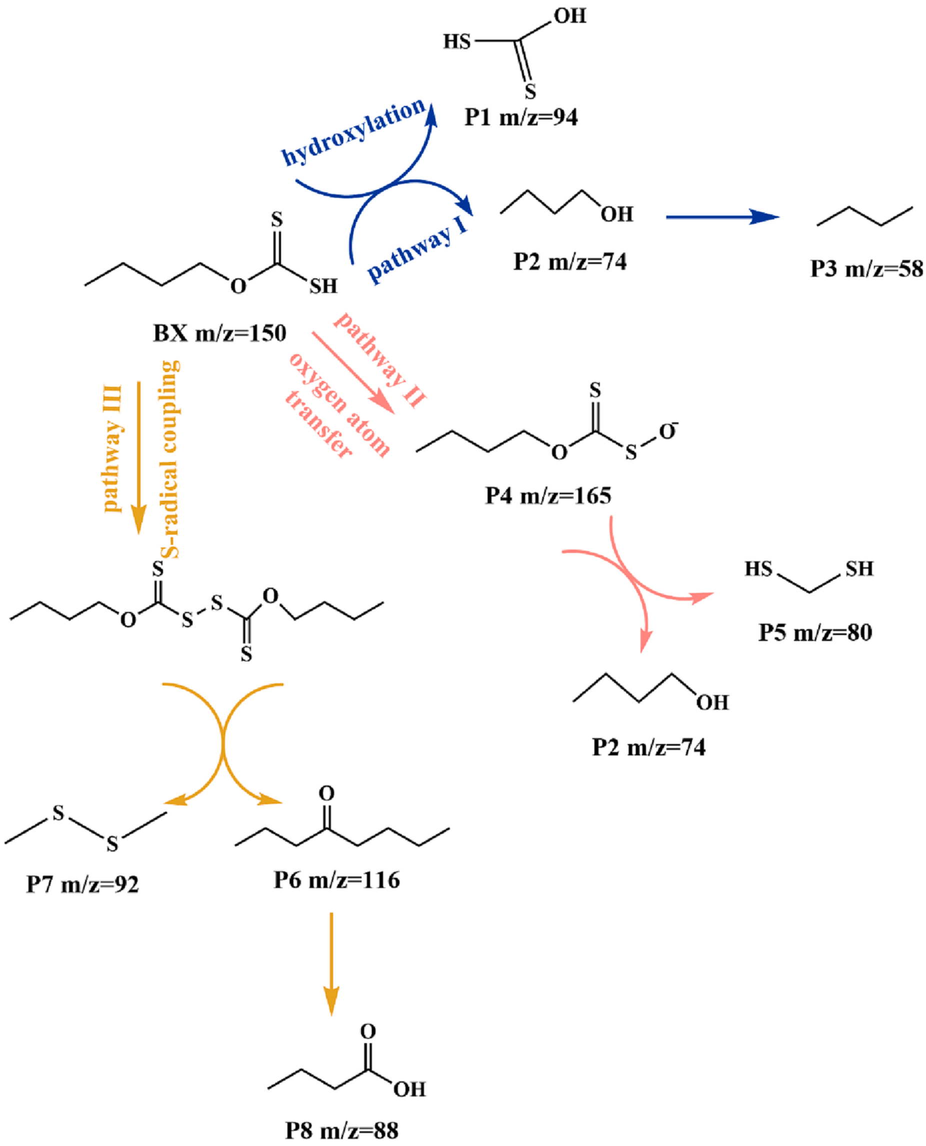

Fig. 8. Proposed degradation routes of BX in the Fe-BC250/PS process.

hydroxylation [10,13]. In general, C—O bonds are more easily attacked than other bonds [48,49], and pathway I was proposed based on this principle. We suppose that the hydroxylation process occurred after C—O bond cleavage, thus producing P1 ($m/z = 94$) and forming P2 ($m/z = 74$) simultaneously, which continued to degrade to form P3 ($m/z = 58$). Interestingly, depending on the target compound structure, Fe(IV) can attack organic compounds through oxygen atom transfer and hydrogen abstraction [50]. P4 ($m/z = 165$) was considered to be the degradation product of BX induced by an oxygen atom transfer step in Fe (IV)-mediated oxidation. P4 was further converted to P2 ($m/z = 74$) and P5 ($m/z = 80$). Fe(IV) can extract hydrogen atoms by attacking S—H bonds via hydrogen abstraction, resulting in the coupling of S radicals. Based on this principle, pathway III was presented. BX first generates double xanthate, which is further degraded; the corresponding products are P6 ($m/z = 116$) and P7 ($m/z = 92$). P6 ($m/z = 116$) is further oxidized to produce P8 ($m/z = 88$). Additionally, to quantitatively describe the BX mineralization degree, the mineralization rate of S and C was calculated using the following formula [51]:

$$\gamma_s = \frac{M_{BX}}{n \times M_{SO_4^{2-}}} \times \frac{C_{SO_4^{2-}}}{C_{BX}} \times 100\% \tag{4}$$

$$\gamma_{TOC} = \frac{TOC_0 - TOC_{30}}{TOC_0} \times 100\% \tag{5}$$

where M_{BX} and $M_{SO_4^{2-}}$ represent the relative molecular masses of BX and SO_4^{2-}, respectively; $C_{SO_4^{2-}}$ is the concentration of SO_4^{2-} in the solution at 30 min; and C_{BX} is the initial BX concentration. Considering that SO_4^{2-} will also be produced after PS decomposition, this part of SO_4^{2-} was subtracted. Thus the final concentration of SO_4^{2-} was 15.25 mg/L. After calculation, γ_s in the Fe-BC250/PS system was equal to 74.7 %, and γ_{TOC} in the Fe-BC250/PS system was 64.7 %. This showed that the Fe-BC250/PS system had high mineralization efficiencies toward C and S.

4. Conclusions

We developed an iron-biochar composite for effective PS activation and BX oxidation over a wide pH range. We further demonstrated the Fe (IV) formation mechanism under alkaline conditions. Under alkaline conditions, the decrease in the solution pH was attributed to hydrolyzed Fe^{2+} generating H^+ and Fe^{2+} combined with OH^- during the reaction, and surface Fe(II) reacted with PS to form Fe(IV). The remaining Fe ion concentration met the standard for sewage discharge into urban sewers

(GB/T 31962-2015). Additionally, the Fe species promoted the formation of the graphitized structure of biochar, and the graphitized structure of biochar accelerated the catalytic oxidative reaction.

The ultra-low-temperature iron-carbon composites had the following characteristics: (i) low inputs of energy and material, and a high catalyst yield; (ii) excellent catalytic performance and rapid degradation of BX with low loading of catalyst (0.1 g/L) and oxidant (PS, 0.1 mmol/L); and (iii) the Fe(IV) pathway was confirmed to be the main mechanism for BX removal in the Fe-BC250/PS system, which exhibited excellent anti-interference capacity toward inorganic anions and natural organics in the natural water environment. Collectively, these findings demonstrate a low-cost and selective remediation system using low-temperature iron-carbon composite catalysts.

Declaration of Competing Interest

The authors declare that they have no known competing financial interests or personal relationships that could have appeared to influence the work reported in this paper.

Data availability

Data will be made available on request.

Acknowledgments

This research was financially supported by the National Key R&D Program of China (2020YFC1807600), the National Natural Science Foundation of China (U20A20323, 52000012), and the Natural Science Foundation of Hunan Province, China (Grant Nos. 2021JJ30123, 2022JJ20009, 2021JJ40578), and the Science and Technology Innovation Program of Hunan Province (2022RC1122).

Appendix A. Supplementary data

Supplementary data to this article can be found online at https://doi.org/10.1016/j.cej.2023.141951.

References

[1] J. Liu, C. Peng, X. Shi, Preparation, characterization, and applications of Fe-based catalysts in advanced oxidation processes for organics removal: A review, Environ. Pollut. 293 (2022), 118565.
[2] Y. Qiu, X. Xu, Z. Xu, J. Liang, Y. Yu, X. Cao, Contribution of different iron species in the iron-biochar composites to sorption and degradation of two dyes with varying properties, Chem. Eng. J. 389 (2020), 124471.
[3] S. Bakshi, C. Banik, S.J. Rathke, D.A. Laird, Arsenic sorption on zero-valent iron-biochar complexes, Water Res. 137 (2018) 153–163.
[4] D. Ma, Y. Yang, B. Liu, G. Xie, C. Chen, N. Ren, D. Xing, Zero-valent iron and biochar composite with high specific surface area via K_2FeO_4 fabrication enhances sulfadiazine removal by persulfate activation, Chem. Eng. J. 408 (2021), 127992.
[5] G. Zhao, J. Zou, X. Chen, L. Liu, Y. Wang, S. Zhou, X. Long, J. Yu, F. Jiao, Iron-based catalysts for persulfate-based advanced oxidation process: Microstructure, property and tailoring, Chem. Eng. J. 421 (2021), 127845.
[6] Z. Wang, J. Jiang, S. Pang, Y. Zhou, C. Guan, Y. Gao, J. Li, Y. Yang, W. Qiu, C. Jiang, Is Sulfate Radical Really Generated from Peroxydisulfate Activated by Iron(II) for Environmental Decontamination? Environ. Sci. Technol. 52 (2018) 11276–11284.
[7] J. Hu, S. Wang, J. Yu, W. Nie, J. Sun, S. Wang, Duet Fe_3C and FeNx Sites for H_2O_2 Generation and Activation toward Enhanced Electro-Fenton Performance in Wastewater Treatment, Environ. Sci. Technol. 55 (2021) 1260–1269.
[8] V.K. Sharma, M. Feng, D.D. Dionysiou, H.C. Zhou, C. Jinadatha, K. Manoli, M. F. Smith, R. Luque, X. Ma, C.H. Huang, Reactive High-Valent Iron Intermediates in Enhancing Treatment of Water by Ferrate, Environ. Sci. Technol. 56 (2022) 30–47.
[9] B. Shao, H. Dong, B. Sun, X. Guan, Role of Ferrate(IV) and Ferrate(V) in Activating Ferrate(VI) by Calcium Sulfite for Enhanced Oxidation of Organic Contaminants, Environ. Sci. Technol. 53 (2019) 894–902.
[10] Y. Zong, Y.F. Shao, Y.Q. Zeng, B.B. Shao, L.Q. Xu, Z.Y. Zhao, W. Liu, D.L. Wu, Enhanced Oxidation of Organic Contaminants by Iron(II)-Activated Periodate: The Significance of High-Valent Iron-Oxo Species, Environ. Sci. Technol. 55 (2021) 7634–7642.
[11] S. Liang, L. Zhu, J. Hua, W. Duan, P.T. Yang, S.L. Wang, C. Wei, C. Liu, C. Feng, Journal of Hazardous MaterialsEnviron Sci Technol.Fe^{2+}/HClO Reaction Produces $Fe^{IV}O^{2+}$: An Enhanced Advanced Oxidation Process, Environ. Sci. Technol. 54 (2020) 6406–6414.
[12] J. Kim, T.Q. Zhang, W. Liu, P.H. Du, J.T. Dobson, C.H. Huang, Advanced Oxidation Process with Peracetic Acid and Fe(II) for Contaminant Degradation, Environ. Sci. Technol. 53 (2019) 13312–13322.
[13] J. Liang, X. Duan, X. Xu, K. Chen, Y. Zhang, L. Zhao, H. Qiu, S. Wang, X. Cao, Persulfate Oxidation of Sulfamethoxazole by Magnetic Iron-Char Composites via Nonradical Pathways: Fe(IV) Versus Surface-Mediated Electron Transfer, Environ. Sci. Technol. 55 (2021) 10077–10086.
[14] Z. Wang, W. Qiu, S. Pang, Y. Gao, Y. Zhou, Y. Cao, J. Jiang, Relative contribution of ferryl ion species (Fe(IV)) and sulfate radical formed in nanoscale zero valent iron activated peroxydisulfate and peroxymonosulfate processes, Water Res. 172 (2020), 115504.
[15] Z. Wang, W. Qiu, S.-Y. Pang, Y. Zhou, Y. Gao, C. Guan, J. Jiang, Further understanding the involvement of Fe(IV) in peroxydisulfate and peroxymonosulfate activation by Fe(II) for oxidative water treatment, Chem. Eng. J. 371 (2019) 842–847.
[16] H. Li, J. Yao, R. Duran, J. Liu, N. Min, Z. Chen, X. Zhu, C. Zhao, B. Ma, W. Pang, M. Li, Y. Cao, B. Liu, Toxic response of the freshwater green algae Chlorella pyrenoidosa to combined effect of flotation reagent butyl xanthate and nickel, Environ. Pollut. 286 (2021), 117285.
[17] D. He, J. Ma, R.N. Collins, T.D. Waite, Effect of Structural Transformation of Nanoparticulate Zero-Valent Iron on Generation of Reactive Oxygen Species, Environ. Sci. Technol. 50 (2016) 3820–3828.
[18] P. Zhang, X. Tan, S. Liu, Y. Liu, G. Zeng, S. Ye, Z. Yin, X. Hu, N. Liu, Catalytic degradation of estrogen by persulfate activated with iron-doped graphitic biochar: Process variables effects and matrix effects, Chem. Eng. J. 378 (2019), 122141.
[19] S. Ye, G. Zeng, X. Tan, H. Wu, J. Liang, B. Song, N. Tang, P. Zhang, Y. Yang, Q. Chen, X. Li, Nitrogen-doped biochar fiber with graphitization from Boehmeria nivea for promoted peroxymonosulfate activation and non-radical degradation pathways with enhancing electron transfer, Appl. Catal. B: Environ. 269 (2020), 118850.
[20] M. Sun, C. Chu, F. Geng, X. Lu, J. Qu, J. Crittenden, M. Elimelech, J.-H. Kim, Reinventing Fenton Chemistry: Iron Oxychloride Nanosheet for pH-Insensitive H_2O_2 Activation, Environmental Science & Technology Letters 5 (2018) 186–191.
[21] Z. Li, Y. Sun, Y. Yang, Y. Han, T. Wang, J. Chen, D.C.W. Tsang, Biochar-supported nanoscale zero-valent iron as an efficient catalyst for organic degradation in groundwater, J. Hazard. Mater. 383 (2020), 121240.
[22] J. Yu, L. Tang, Y. Pang, G. Zeng, J. Wang, Y. Deng, Y. Liu, H. Feng, S. Chen, X. Ren, Magnetic nitrogen-doped sludge-derived biochar catalysts for persulfate activation: Internal electron transfer mechanism, Chem. Eng. J. 364 (2019) 146–159.
[23] C.Q. Tan, Q.L. Xu, T.Y. Sheng, X.X. Cui, Z.R. Wu, H.Y. Gao, H. Li, Reactive oxygen species generation in FeOCl nanosheets activated peroxymonosulfate system: Radicals and non-radical pathways, J. Hazard. Mater. 398 (2020).
[24] J. Zhang, G. Zhang, Q.H. Ji, H.C. Lan, J.H. Qu, H.J. Liu, Carbon nanodot-modified FeOCl for photo -assisted Fenton reaction featuring synergistic in-situ H2O2 production and activation, Appl. Catal. B-Environ. 266 (2020).
[25] Y.Q. Chen, Y.P. Liu, L. Zhang, P.C. Xie, Z.P. Wang, A.J. Zhou, Z. Fang, J. Ma, Efficient degradation of imipramine by iron oxychloride-activated peroxymonosulfate process, J. Hazard. Mater. 353 (2018) 18–25.
[26] A. Georgi, M. Velasco Polo, K. Crincoli, K. Mackenzie, F.D. Kopinke, Accelerated Catalytic Fenton Reaction with Traces of Iron: An Fe-Pd-Multicatalysis Approach, Environ. Sci. Technol. 50 (2016) 5882–5891.
[27] Y. Lei, C.S. Chen, Y.J. Tu, Y.H. Huang, H. Zhang, Heterogeneous Degradation of Organic Pollutants by Persulfate Activated by CuO-Fe_3O_4: Mechanism, Stability, and Effects of pH and Bicarbonate Ions, Environ. Sci. Technol. 49 (2015) 6838–6845.
[28] B. Wang, C. Zhu, D. Ai, Z. Fan, Activation of persulfate by green nano-zero-valent iron-loaded biochar for the removal of p-nitrophenol: Performance, mechanism and variables effects, J. Hazard. Mater. 417 (2021), 126106.
[29] J. Wang, S. Wang, Reactive species in advanced oxidation processes: Formation, identification and reaction mechanism, Chem. Eng. J. 401 (2020), 126158.
[30] S. Ye, G. Zeng, X. Tan, H. Wu, J. Liang, B. Song, N. Tang, P. Zhang, Y. Yang, Q. Chen, X. Li, Nitrogen-doped biochar fiber with graphitization from Boehmeria nivea for promoted peroxymonosulfate activation and non-radical degradation pathways with enhancing electron transfer, Appl. Catal. B: Environ. 269 (2020).
[31] G. Wang, X. Nie, X. Ji, X. Quan, S. Chen, H. Wang, H. Yu, X. Guo, Enhanced heterogeneous activation of peroxymonosulfate by Co and N codoped porous carbon for degradation of organic pollutants: the synergism between Co and N, Environmental Science, Nano 6 (2019) 399–410.
[32] W. Ren, C. Cheng, P. Shao, X. Luo, H. Zhang, S. Wang, X. Duan, Origins of Electron-Transfer Regime in Persulfate-Based Nonradical Oxidation Processes, Environ. Sci. Technol. 56 (2022) 78–97.
[33] C. Tan, Q. Xu, T. Sheng, X. Cui, Z. Wu, H. Gao, H. Li, Reactive oxygen species generation in FeOCl nanosheets activated peroxymonosulfate system: Radicals and non-radical pathways, J. Hazard. Mater. 398 (2020), 123084.
[34] J. Liang, L. Fu, K. Gao, X. Duan, Accelerating radical generation from peroxymonosulfate by confined variable Co species toward ciprofloxacin mineralization: ROS quantification and mechanisms elucidation, Appl. Catal. B: Environ. 315 (2022), 121542.
[35] L. Peng, X. Duan, Y. Shang, B. Gao, X. Xu, Engineered carbon supported single iron atom sites and iron clusters from Fe-rich Enteromorpha for Fenton-like reactions via nonradical pathways, Appl. Catal. B: Environ. 287 (2021), 119963.
[36] Y. Li, T. Yang, S. Qiu, W. Lin, J. Yan, S. Fan, Q. Zhou, Uniform N-coordinated single-atomic iron sites dispersed in porous carbon framework to activate PMS for

efficient BPA degradation via high-valent iron-oxo species, Chem. Eng. J. 389 (2020), 124382.

[37] S. Ye, W. Xiong, J. Liang, H. Yang, H. Wu, C. Zhou, L. Du, J. Guo, W. Wang, L. Xiang, G. Zeng, X. Tan, Refined regulation and nitrogen doping of biochar derived from ramie fiber by deep eutectic solvents (DESs) for catalytic persulfate activation toward non-radical organics degradation and disinfection, J. Colloid Interface Sci. 601 (2021) 544–555.

[38] H. Li, C. Shan, B. Pan, Fe(III)-Doped g-C_3N_4 Mediated Peroxymonosulfate Activation for Selective Degradation of Phenolic Compounds via High-Valent Iron-Oxo Species, Environ. Sci. Technol. 52 (2018) 2197–2205.

[39] X. Peng, J. Wu, Z. Zhao, X. Wang, H. Dai, L. Xu, G. Xu, Y. Jian, F. Hu, Activation of peroxymonosulfate by single-atom Fe-g-C_3N_4 catalysts for high efficiency degradation of tetracycline via nonradical pathways: Role of high-valent iron-oxo species and Fe–Nx sites, Chem. Eng. J. 427 (2022), 130803.

[40] L. Lai, H. Zhou, H. Zhang, Z. Ao, Z. Pan, Q. Chen, Z. Xiong, G. Yao, B. Lai, Activation of peroxydisulfate by natural titanomagnetite for atrazine removal via free radicals and high-valent iron-oxo species, Chem. Eng. J. 387 (2020), 124165.

[41] E. Sediva, T. Defferriere, N.H. Perry, H.L. Tuller, J.L.M. Rupp, In Situ Method Correlating Raman Vibrational Characteristics to Chemical Expansion via Oxygen Nonstoichiometry of Perovskite Thin Films, Adv. Mater. 31 (2019) e1902493.

[42] J.Y. Chen, L. Dang, H. Liang, W. Bi, J.B. Gerken, S. Jin, E.E. Alp, S.S. Stahl, Operando Analysis of NiFe and Fe Oxyhydroxide Electrocatalysts for Water Oxidation: Detection of Fe^{4+} by Mossbauer Spectroscopy, J. Am. Chem. Soc. 137 (2015) 15090–15093.

[43] H. Dong, Y. Li, S. Wang, W. Liu, G. Zhou, Y. Xie, X. Guan, Both Fe(IV) and Radicals Are Active Oxidants in the Fe(II)/Peroxydisulfate Process, Environ. Sci. Technol. Letters 7 (2020) 219–224.

[44] H. Dong, Q. Xu, L. Lian, Y. Li, S. Wang, C. Li, X. Guan, Degradation of Organic Contaminants in the Fe(II)/Peroxymonosulfate Process under Acidic Conditions: The Overlooked Rapid Oxidation Stage, Environ. Sci. Technol. 55 (2021) 15390–15399.

[45] D. Cheng, S. Yuan, P. Liao, P. Zhang, Oxidizing Impact Induced by Mackinawite (FeS) Nanoparticles at Oxic Conditions due to Production of Hydroxyl Radicals, Environ. Sci. Technol. 50 (2016) 11646–11653.

[46] M. Jiang, M.H. Zhang, L.Z. Wang, Y.W. Fei, S. Wang, A. Nunez-Delgado, A. Bokhari, M. Race, A. Khataee, J.J. Klemes, L.B. Xing, N. Han, Photocatalytic degradation of xanthate in flotation plant tailings by TiO2/graphene nanocomposites, Chem. Eng. J. 431 (2022).

[47] S.Z. Yang, H.N. Sun, S.P. Su, G.H. Han, Y.F. Huang, Fabrication, characterizations and performance of a high-efficiency micro-electrolysis filler for isobutyl xanthate (IBX) degradation, J. Hazard. Mater. 403 (2021).

[48] S. Yang, H. Sun, S. Su, G. Han, Y. Huang, Fabrication, characterizations and performance of a high-efficiency micro-electrolysis filler for isobutyl xanthate (IBX) degradation, J. Hazard. Mater. 403 (2021), 123640.

[49] M. Jiang, M. Zhang, L. Wang, Y. Fei, S. Wang, A. Núñez-Delgado, A. Bokhari, M. Race, A. Khataee, J. Jaromír Klemeš, L. Xing, N. Han, Photocatalytic degradation of xanthate in flotation plant tailings by TiO_2/graphene nanocomposites, Chem. Eng. J. 431 (2022), 134104.

[50] Y. Zong, X. Guan, J. Xu, Y. Feng, Y. Mao, L. Xu, H. Chu, D. Wu, Unraveling the Overlooked Involvement of High-Valent Cobalt-Oxo Species Generated from the Cobalt(II)-Activated Peroxymonosulfate Process, Environ. Sci. Technol. 54 (2020) 16231–16239.

[51] M. Li, H. Zhong, Z. He, L. Hu, W. Sun, P. Loganathan, D. Xiong, Degradation of various thiol collectors in simulated and real mineral processing wastewater of sulfide ore in heterogeneous modified manganese slag/PMS system, Chem. Eng. J. 413 (2021), 127478.